ARTICLE IN PRESS

Microstructural characterization of dental zinc phosphate cements using combined small angle neutron scattering and microfocus X-ray computed tomography

Alberto Viani[a,], Konstantinos Sotiriadis[a], Ivana Kumpová[a], Lucia Mancini[b], Marie-Sousai Appavou[c]*

[a] *Institute of Theoretical and Applied Mechanics AS CR, Centre of Excellence Telč, Batelovská 485, CZ-58856 Telč, Czechia*

[b] *Elettra-Sincrotrone Trieste S.C.p.A., S.S. 14-km 163.5 Area Science Park, 34149 Trieste, Basovizza, Italy*

[c] *Forschungszentrum Jülich GmbH, Jülich Centre for Neutron Science JCNS, Aussenstelle am MLZ, Lichtenbergstraße 1, 85747 Garching, Germany*

ARTICLE INFO

ABSTRACT

Objective. To characterize the microstructure of two zinc phosphate cement formulations in order to investigate the role of liquid/solid ratio and composition of powder component, on the developed porosity and, consequently, on compressive strength.

Methods. X-ray powder diffraction with the Rietveld method was used to study the phase composition of zinc oxide powder and cements. Powder component and cement microstructure were investigated with scanning electron microscopy. Small angle neutron scattering (SANS) and microfocus X-ray computed tomography (XmCT) were together employed to characterize porosity and microstructure of dental cements. Compressive strength tests were performed to evaluate their mechanical performance.

Results. The beneficial effects obtained by the addition of Al, Mg and B to modulate powder reactivity were mitigated by the crystallization of a Zn aluminate phase not involved in the cement setting reaction. Both cements showed spherical pores with a bimodal distribution at the micro/nano-scale. Pores, containing a low density gel-like phase, developed through segregation of liquid during setting. Increasing liquid/solid ratio from 0.378 to 0.571, increased both SANS and XmCT-derived specific surface area (by 56% and 22%, respectively), porosity (XmCT-derived porosity increased from 3.8% to 5.2%), the relative fraction of large pores $\geq 50\,\mu m$, decreased compressive strength from $50 \pm 3\,MPa$ to $39 \pm 3\,MPa$, and favored microstructural and compositional inhomogeneities.

Significance. Explain aspects of powder design affecting the setting reaction and, in turn, cement performance, to help in optimizing cement formulation. The mechanism behind

development of porosity and specific surface area explains mechanical performance, and processes such as erosion and fluoride release/uptake.

1. Introduction

Zinc phosphate cements are a class of acid-base cements which find application in dentistry largely as luting or lining agents [1]. ZPC is one of the oldest dental cements, being introduced in the 1880s. Because of the inferior mechanical and biological properties, compared to some of the more recent bioactive restorative materials [2,3], the use of ZPC has significantly declined, although it possesses a successful track record, supported by clinical evidences [4,5]. However, a huge resident population of cemented restorations still exists, making the understanding of structure-limited properties important for the interpretation of their clinical longevity. ZPC is supplied as a liquid component, consisting in a solution of phosphoric acid (45–65%) containing up to about 3% of aluminum and possibly zinc (up to 10%), and a zinc oxide powder. Additions to the solution are aimed at gaining control over the reaction rate and the heat of reaction. Reactivity of the powder is reduced by annealing ZnO at temperatures between 1000 °C and 1400 °C, after mixing it with about 10 wt% of MgO. Sometimes, fluxing agents, like borax, are added to improve the degree of sintering [6]. In analogy with MgO employed in magnesium phosphate cements [7], the thermal treatment results in ZnO of higher mean crystallite size and particles with smooth surface [8,9]. With these compositions, the first product of the setting reaction is completely amorphous, and the presence of aluminum has been recognized to play a crucial role in modifying the chemistry of the reaction and stabilize the amorphous fraction [10–12].

The study of the setting reaction showed that this first product is an amorphous zinc phosphate hydrate which forms at the surface of the ZnO particles [11]. Crystallization of zinc phosphate is thought to be hindered by the disorder introduced by the polymeric complexes formed when Al is introduced in the phosphoric acid solution [12] or by the entanglement of chains of aluminum phosphate hydrogel embedding the particles [11]. In the latter case, the experimental evidences pointed to an amorphous zinc phosphate with composition $Zn_2P_4O_{12}\cdot 8H_2O$, a cyclophosphate in which some of the water molecules are loosely bound. This was found consistent with the crystallization of hopeite ($Zn_3(PO_4)_2\cdot 2H_2O$) from the amorphous, an occurrence observed in aged commercial cements [13,14]. The compressive strength of the cement was shown to increase with the increase in the powder fraction [15–17] up to values above which probably the wetting of ZnO particles is compromised, in analogy with other dental cements [18]. In the clinical practice, the liquid to solid weight ratio (l/s) is optimized for the specific applications, therefore, variable amounts of unreacted ZnO can be found in the final cement [10,16]. It follows that the ZPC can be considered as a composite material and the interaction between ZnO grains and the amorphous matrix has important implications for the longevity of the restoration. In this respect, crack deflection around composite particles, a well-documented toughening mechanism [19,20], has been observed in ZPCs [16].

On the other hand, pores are fracture initiation sites under load [21,22], although, in glass materials they are considered more stress concentrators rather than flaws, as for polycrystalline or glass-ceramics [23]. In general, since ZPCs are highly defect-limited, the measure of the porosity is a significant parameter for their characterization. The final porosity of the cement can be strongly affected by the mixing technique adopted and the viscosity of the paste (dependent on l/s) during preparation [18,24,25]. The imperfect homogenization of the powder was found to yield clusters of ZnO particles which develop large irregular pores with diameter $D > 5\,\mu m$ [16] of deleterious nature [23]. In this respect, a distinction should be made between the large pores (>1 μm in size) and the smaller meso-micro-pores (as defined in Ref. [26]). In fact, the amount of the former has been directly related to the cases of failure of the restorations and, in general, was found to correlate negatively with the mechanical properties [21,24]. Much less information is available about the latter. Few examples of characterization of porosity in ZPCs are reported [16,27,28], in some of them optical techniques were used [16,27], which show obvious limits of representativeness and accessible range in pore size. A technique usually employed to retrieve the pore-size distribution in solids is mercury intrusion porosimetry (MIP). However, MIP possess several drawbacks that can sometimes lead to misleading results [29]; it is destructive, it relies on the assumption of cylindrical pore shape and it is limited to the detection of open porosity [30]. Reliability of MIP results might be also impaired by microstructural changes occurring in the sample under the vacuum conditions required for the analysis. Substantial loss of chemically bound water in the porosimeter has been observed in magnesium phosphate cements [31]. Furthermore, availability of MIP for the next future is threatened by the progressive mercury phase out ratified by many countries in 2013 [32].

In any porous material, a further critical descriptive parameter of its microstructure is the S_V specific surface area. Being related to the degree of subdivision, it is most sensitive to changes in the smallest microstructural details and controls to a large extent the rate of the chemical and/or physicochemical reactions, therefore the behavior of the material in applications. Dissolution/erosion, take up or release of elements from solution (such as fluoride) are of interest for restorative materials, and they have been shown to be more surface-dependent rather than volume-dependent [33].

SANS has been recognized to be a valuable tool for the evaluation and quantification of a statistically representative microstructure (and nano-structure) of heterogeneous materials. It has been successfully applied to porous solids, such as ceramics [34], and, recently, acid-base cements [31,35]. The

microstructure can be proved for a volume defined by the beam spot size (of the order of 5–10 mm) and the sample thickness (up to few mm). The advantages of using neutrons are that, thanks to their high depth of penetration, they can probe the microstructure in the entire volume of sample (e.g. open and closed porosity), the measurement is not perturbing the sample, and no special sample preparation is required.

XmCT is a powerful non-destructive 3-D imaging technique for characterizing the microstructure and morphology of materials. The high contrast and spatial resolution of the obtained images allow for visualization and quantification of porosity and pore-size distribution without any hypothesis on pore geometry. XmCT has been widely used in dental research [36], however there are few examples in literature concerning the investigation of restorative dental materials [24,37,38]. Depending on the experimental setup, SANS allows for gaining access to the porosity from the nano-scale up to about 1 μm, whereas with XmCT, this range is typically shifted towards larger pore sizes, from around 1 μm up to several mm. It follows that the combination of the two techniques, by making accessible a wide range in porosity, greatly enhances our capability of describing sample microstructure.

In this work, the microstructure of two ZPC formulations of the same product, prepared according to manufacturer's recommendations, has been investigated in order to provide insights into the role of l/s and composition of powder component on the developed porosity and, consequently, on compressive strength. The morphology of ZnO grains and the phase composition of zinc oxide powder and ZPC have been investigated with a combination of analytical techniques, including XRPD with the Rietveld method and SEM. Pore-size distribution, porosity and S_V have been derived from the analysis of SANS data. The volume-weighted size distribution of pores has been calculated through a procedure of profile fitting of the curves. Pore structure was visualized, and from the analysis of reconstructed 3-D images of the two ZPC samples, produced from the tomographic projections collected with XmCT, porosity and S_V have been calculated. Compressive strength was determined according to the standard EN ISO 9917-1:2007 [39].

2. Materials and methods

2.1. Materials

A commercially obtained ZPC product (Adhesor, SpofaDental a.s., Jičín, Czech Republic; LOT 5412375) was employed to prepare two cements, recommended as filling and fixed bridge bonding materials. They have been prepared 2 weeks after purchase and within the first year out of the five years expiry period. The compositions, labelled Z1 and Z2, with l/s = 0.348 and 0.571, respectively, have been hand mixed on a chilled glass pad with a stainless steel spatula. Both tools were kept in refrigerator at 4 °C for 1 h, then left to heat up in air to reach temperature above the dew point (15–18 °C) and carefully dried to prevent moisture contamination. In line with manufacturer's instructions, the powder was added to the liquid in five increments (approx. 200 mg each) while mixing. The entire procedure was accomplished at ambi-

Table 1 – Number of replicates employed for each test and for each studied material.

Sample	XRPD	SEM	SANS	XmCT	Compressive strength
ZP	1	1	–	–	–
Z1	1	3	1	1	5
Z2	1	3	1	1	5

ent temperature of 22 ± 2 °C and 60 ± 3% relative humidity. Specimens were casted in form of discs (2 mm thick, 10 mm diameter) and cylinders (3.8 mm diameter, about 20 mm height), sealed in plastic bags, and cured at 37 °C for 3 days at 60 ± 3% relative humidity. Discs were employed for XRPD and SANS measurements, as well as for SEM observations, while cylinders for XmCT. ZPC specimens used for compressive strength tests were prepared in accordance with the standard EN ISO 9917-1:2007 [39]. The number of replicates employed for each test and studied material are summarized in Table 1. The time interval between samples preparation and testing was 3 days for SANS and XmCT, and 1 week for XRPD and SEM. The latter longer time interval was observed also in order to evaluate the potential crystallization of phases like hopeite in the bulk cement.

2.2. Analytical methods

Samples of ZPC and zinc oxide powder for XRPD data collection were ground by hand in an agate mortar and mounted on an Al sample holder using the side loading technique to minimize a priori preferred orientation of crystallites. Analytical grade ZnO (Merck) was also analyzed for comparison with zinc oxide powder. XRPD data were collected in the angular range 4–82° 2θ at 40 kV and 40 mA using a Bragg–Brentano θ–θ diffractometer (Bruker D8 Advance, Cu Kα radiation (λ = 1.5418 Å)), equipped with a LynxEye 1-D silicon strip detector. Divergence 0.6 mm slits and 2.5° Soller slits were mounted on the incident beam pathway. The pathway of the diffracted beam included a Ni filter and Soller slits (2.5°). A virtual step scan of 0.0102° 2θ, with 0.4 s/step counting time, was employed. Samples were allowed to spin at 15 rpm to improve particle statistics. Quantitative phase analysis (QPA) including both amorphous and crystalline fraction was performed with the Rietveld method by spiking the sample with 10 wt% of internal standard (NIST SRM 676a). Refinements were accomplished with the TOPAS 4.2 software (Bruker AXS).

SEM observations were performed at 20 kV accelerating voltage on the powder and the freshly exposed internal surface of ZPC samples mounted on aluminum stubs and coated with 5 nm thick gold film, employing a FEI QUANTA FEG 450 instrument equipped with an EDAX Apollo X energy dispersive detector, whose window is capable of detecting all chemical elements down to beryllium. EDS analysis was performed on 12 points for each sample.

The sample discs were mounted between two quartz windows for SANS data collection. SANS curves were recorded at the KWS-2 instrument [40] operated by JCNS at the Heinz Maier–Leibnitz Zentrum MLZ (Garching, Germany). The Q range (0.025–3.15 nm^{-1}) was covered by merging data collected at wavelength λ = 5.151 Å with sample-to-detector distance

2.23 m and 7.73 m, and at wavelength $\lambda = 10.308$ Å with sample-to-detector distance 19.43 m. Time for data collection was 5 min for each Q range. The scattering intensity was obtained as a function of momentum transfer Q:

$$Q = \frac{4\pi}{\lambda} \sin 2\theta \qquad (1)$$

where 2θ is the scattering angle. Data were collected with a 2-D detector and radially averaged in order to obtain 1-D intensity patterns. The 2-D raw data have been corrected for beam attenuation (according to measured sample thickness), the scattering from the empty cell, the electronic and background noise. Intensity was calibrated against a plexiglass standard material to set the data to absolute scale. Sample thickness was chosen in order to minimize multiple scattering effects.

Details of the SANS theory may be found elsewhere [41], here only few concepts are summarized. SANS can be described as the Fourier transform of the fluctuation in scattering length density (a measure of the interaction of neutrons with matter) within the sample. In a porous solid, when the difference in scattering density originates from the boundary between the pores and the surrounding matrix, the single phase approximation is usually made and the system is treated as biphasic [42]. The complex microstructure is usually described assuming pores of spherical shape [43]. According to the Bragg law, the size of detected features in a SANS experiment is inversely proportional to Q, thus, large structures will be visible at small Q. The upper limit in distance periodicity d is thus defined by the lowest Q value accessible to the experiment according to:

$$d = \frac{2\pi}{Q} \qquad (2)$$

Commonly, in the limit of high Q, in dense systems with sharp and smooth pore surfaces, the scattering curve exhibits a single power law obeying the Porod law [44]. Therefore, the curve can be fitted with the equation:

$$I(Q) = 2\pi S_V K^2 \left(\frac{1}{Q}\right)^4 + C \qquad (3)$$

The exponent in Eq. (3) identifies the slope of the SANS curve, K is the previously mentioned scattering contrast within the sample (that can be calculated from the chemical composition) and C is a constant background. From these considerations it follows that the scattered intensity becomes proportional to S_V. A change in slope of the SANS curve, marks the boundary between different regimes, characterized by different length scales. This allows for the identification of different scattering regimes, but, since the scattering profile contains information on the shape and size distribution of the scatterers, it is possible to retrieve the particle-size distribution of the scattering objects. In this paper, this quantity has been obtained with the software McSAS [45], implementing a fitting procedure based on the Monte Carlo method, applying the sphere model for the pore shape.

XmCT analyses were carried out using the TomoLab instrument custom-developed at the Elettra synchrotron light laboratory in Trieste (Italy). The employed instrument is based on a microfocus Hamamatsu L9181 X-ray source, which guarantees a minimum focal spot size of 5 μm, in a voltage range from 40 up to 130 kV and a maximum current of 300 μA. A 12 bit, water-cooled, Photonic Science VHR CCD camera with a maximum field of view of 49.9×33.2 mm^2 and a pixel size of 12.5 μm was used as detector system [46,47]. Data were collected at a voltage of 130 kV, a current of 61 μA, with a source-to-sample distance $D1 = 80$ mm and a sample-to-detector distance $D2 = 400$ mm corresponding to an effective pixel size of 5.0 μm (pixel binning $= 2 \times 2$). Each tomographic scan was performed rotating the sample over 360° and recording 1440 projections with an exposure time/projection of 7 s. The pathway of the incident X-ray beam included a 1.5 mm thick Al filter. The scanning procedure adopted for these XmCT measurements corresponds to phase-contrast modality in edge-detection regime [48,49].

Slice reconstruction was obtained by using the commercial software COBRA (Exxim). The COBRA software was also used to reduce beam hardening artefacts from the reconstructed images while for ring artefacts removal a filter, implemented in the *Pore3D* software library developed at Elettra, was applied directly to the reconstructed slices [50,51]. The commercial software VG Studio Max 3.0 was employed for the 3-D rendering, the image analysis, and the extraction of numerical data for both samples. The 3-D analysis was performed on Volumes of Interest (VOIs) of the same size ($368 \times 398 \times 929$ voxels; isotropic voxel size $= 5$ μm, volume of 17.00 mm^3) cropped from the center of the reconstructed volumes of each sample. This step allowed excluding the regions close to the sample borders of the pseudo-cylindrical sample from the subsequent analysis. The VOI was chosen as the largest possible from the original data set, in order to be representative of the whole sample. The quality of the analysis of porosity depends also on the number of voids included in the VOI. In this case, considering that the voids are small with respect to the VOI size, and their total number of the order of 10^4, a satisfactory statistical consistency can be assumed. An appropriate threshold Iso value, below which the density of the material is considered virtually zero, i.e. the corresponding volume is considered as pore, was set for each sample. The choice of the optimal value was done with the aid of the automatic definition routine implemented in the software and visually verified on several slices. Low level Gauss adaptive digital filtering, available from the VGDefX algorithm of the software, was applied on VOIs to reduce the noise of the data set before thresholding, in order to preserve the pore shape. The obtained threshold values were 100.5 and 76.0 for the samples Z1 and Z2, respectively. Interactive output of the software, showing the histograms with the threshold Iso values, is reported as Supplementary material Fig. S1. The objects considered as pores in a meaningful way and included in porosity calculations, were those with size larger than 8 voxels (volume of 1.0×10^{-6} mm^3). A total number of 26324 and 25729 pores for Z1 and Z2 samples, respectively, were used in the analysis. The calculation of porosity was performed processing voxel data sets according to the standard VDG P201 [52]. Therefore, pore radius/diameter and the corresponding S_V were calculated considering the circumscribed sphere of the pore.

Table 2 – Quantitative phase analysis of zinc oxide powder (ZP) and ZPC samples (Z1 and Z2). Phase fractions are in wt%.					
Sample	Zincite ZnO	Periclase MgO	Gahnite $ZnAl_2O_4$	Kotoite $Mg_3B_2O_6$	Amorphous
ZP	83.5 ± 0.2	1.2 ± 0.1	2.8 ± 0.1	6.1 ± 0.1	6.5 ± 0.9
Z1	45.2 ± 0.2	0.4 ± 0.1	1.8 ± 0.1	3.6 ± 0.1	49.1 ± 0.4
Z2	34.7 ± 0.2	0.6 ± 0.1	1.8 ± 0.1	3.2 ± 0.1	59.8 ± 0.3
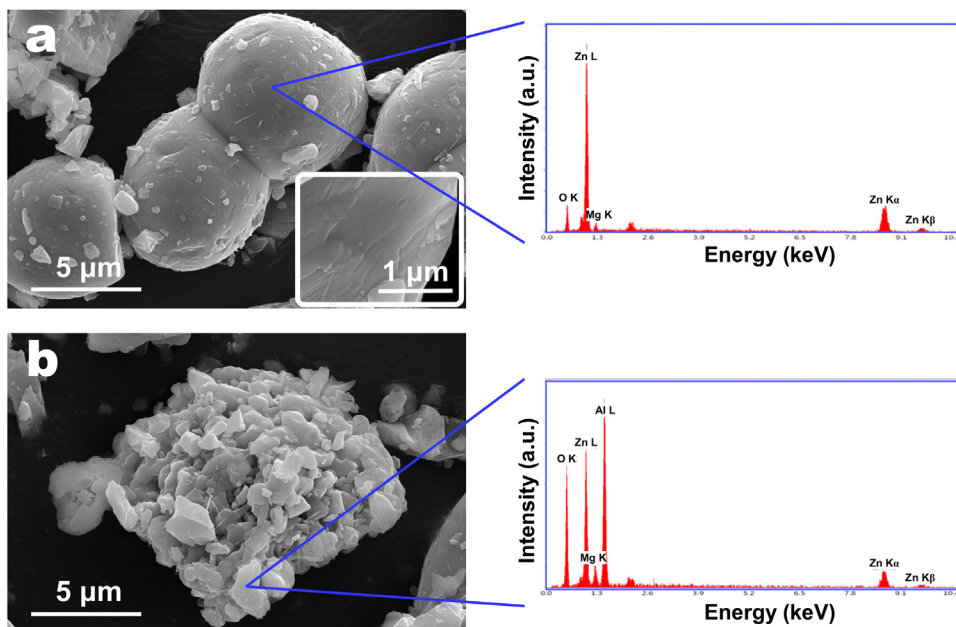
Fig. 1 – SEM micrographs of powder component with results of EDS point analysis. ZnO round shaped grains with some Mg content in (a), an agglomerate of small particles largely composed of gahnite in (b). Inset in (a) depicts the internal surface of a fractured grain at higher magnification. Labels in the graphical representation of EDS spectra identify detected elements. Peak at 2.12 keV is due to the signal from gold coating.

Compressive strength was determined according to the standard EN ISO 9917-1:2007 [39], averaging the values obtained from 5 samples for each ZPC composition.

3.   Results

Results of the Rietveld refinements of zinc oxide powder and ZPC samples are summarized in Table 2. Reported standard deviations are obtained from the refinement procedure. Graphical output of the Rietveld refinements is given as Supplementary material Figs. S2 and S3. Zincite (ZnO) is by far the most abundant phase detected in the zinc oxide powder, while gahnite ($ZnAl_2O_4$), periclase (MgO) and kotoite ($Mg_3B_2O_6$) have been identified in lower percentages. It is worth noting that a small amount of an amorphous phase was also detected. As expected, the amorphous fraction is the most abundant phase in the ZPC samples. A fraction of unreacted ZnO is still present, in higher amount when less liquid was employed. The other phases of the powder component have been also detected; their amount is similar in the two samples.

Fig. 1 reports selected SEM micrographs and two examples of EDS point analysis of the powder component. ZnO grains are sub spherical with a relatively smooth surface. Several examples of grain coalescence, as shown in Fig. 1a, were observed. Internal surface of crushed grains is compact with

Table 3 – Microstructural parameters of ZnO from the powder (ZP) and analytical grade ZnO (ZM) as obtained from Rietveld refinements.			
Sample	a (Å)	c (Å)	L_{Vol}-IB (nm)
ZP	3.2528 ± 0.0001	5.1945 ± 0.0001	663 ± 92
ZM	3.2499 ± 0.0001	5.2068 ± 0.0002	126 ± 5

no detectable porosity (inset in Fig. 1a). The elemental analysis reveals that some Mg was incorporated into the zincite structure. The powder is largely composed of the round shaped ZnO particles with a minor amount of aggregates of smaller grains containing mainly the spinel gahnite, as depicted in Fig. 1b. Elemental analysis showed that Mg was also hosted into the structure of the spinel.

Table 3 reports the crystallographic and microstructural parameters obtained from the Rietveld refinement of zincite in the powder component and of analytical grade ZnO (Merck). Examples of ZnO residual grains and porosity in the matrix of ZPC under SEM analysis, are illustrated in Fig. 2. Both ZPC samples share the same microstructural features, with the grains of unreacted ZnO embedded in an apparently amorphous matrix (Fig. 2a). At low magnification, the unreacted grains, few μm in size, are homogeneously distributed and more abundant in the sample Z1, in accordance with the ZPC formulations. Their exposed surface is irregular, with numerous etch pits (Fig. 2a), result of the reaction with the acid
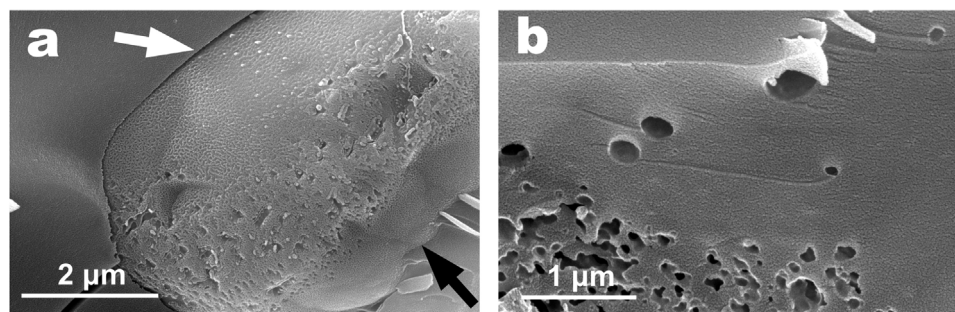
Fig. 2 – SEM micrographs of ZPC cement fractured surfaces. A detail of a ZnO residual grain in the ZPC matrix is displayed in (a), whereas a typical example of porosity in the amorphous matrix is depicted in (b). Detail of the original contact with the matrix (black arrow) and detachment induced by sample preparation (white arrow) are shown.

phosphate solution. The contact with the matrix is in perfect continuity (black arrow in Fig. 2a); partial detachment (white arrow in Fig. 2a) and some cracks observed in the matrix were likely induced by the mechanical action exerted on the sample to expose the internal surface. The observed porosity was concentrated in the matrix and consisted of spherical and sub-spherical pores, with no marked shape anisotropy, locally coalescing, as shown in Fig. 2b. The internal surface of pores appears smooth.

Fig. 3 depicts $\log I(Q)$ vs. $\log Q$ plots of the SANS curves of the investigated samples and the result of the best fits obtained using the Monte Carlo method. A graphical representation of the volume-weighted pore-size distributions associated with the fit of the curves is reported in Fig. 4.

Cross-sectional 2-D XmCT images of the two ZPC samples are shown in Fig. 5. Cracks, connecting pores or starting from them, are observed more frequently in sample Z2 (a typical example is indicated by arrow in Fig. 5). At a qualitative

level, the general contrast observed in sample Z1 is higher with a higher average Iso value with respect to Z2. This is the consequence of a higher concentration of ZnO grains (more absorbing) in the former. The matrix in Z1 appears more compact than that in Z2; it contains few large pores and a large number of small pores. Notably, in Z2, large pores, which would theoretically be the most detrimental, prevail, and areas with different average grey levels, reflecting density inhomogeneities in the matrix, are observed. They are oriented sub-parallel to the maximum elongation of the samples, and thus, to the mold walls. Their size spans from tens of μm in the horizontal direction to several mm in the vertical direction. These features identify portions of the sample with different X-ray absorption, and they are visible thanks to XmCT, which provides this level of information in the whole volume investigated. It is worth noting that an inhomogeneous distribution of contrast is also observed in the pore volume, irrespective
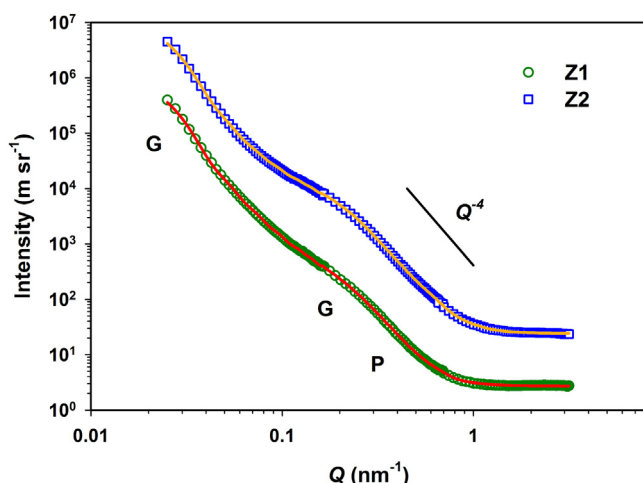
Fig. 3 – SANS curves of Z1 (empty circles) and Z2 (empty squares) samples. Corresponding best fits obtained from McSAS software using Monte Carlo method are reported as continuous lines. For sake of clarity, data of sample Z2 have been multiplied by 10, resulting in a mere vertical shift of the scattering curve. Slope with power law Q^{-4} is reported. Symbols G and P mark Guinier and Porod regimes, respectively.
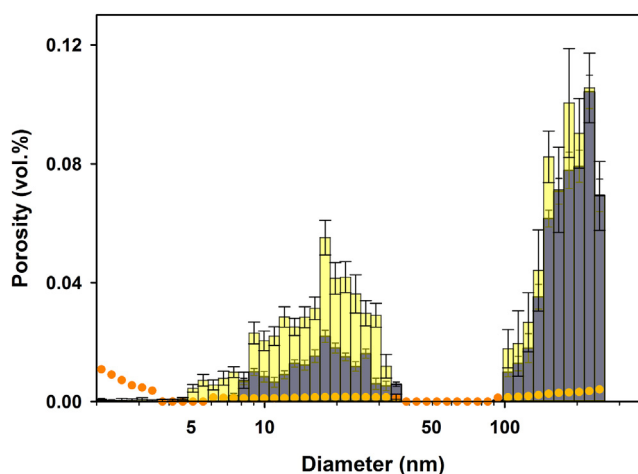
Fig. 4 – Volume-weighted size distributions of pores associated with the Monte Carlo fit of SANS curves. Data from sample Z1 (dark color) are superimposed to Z2 (light color). Error bars are indicated. Dots define the "minimum observability limit" for each contribution, that is, the minimum volume fraction of scatterers required to make a measurable contribution to the scattering pattern (i.e. a contribution exceeding the measurement uncertainty) as defined in Ref. [45].

of pore size. Pore sections (see Fig. 6) reveal features covering the surface of pores, and frequently, with irregular pseudo-dendritic shape in the pore volume.

In Figs. 7 and 8, 3-D renderings showing only the pores identified in the VOI of the two samples, are presented. Four pore-volume intervals, covering the range 1.1×10^{-6}–2.2×10^{-2} mm^3 (corresponding to a range in diameter 0.01–0.28 mm), have been selected to visualize the differences between the samples. As can be qualitatively deduced, pores of lower volume are more abundant in Z1 (Fig. 7), while the number of pores of higher volume is larger in Z2 (Fig. 8), confirming what observed in the slices reported in Fig. 5. The pore shape is spherical to sub-spherical in both samples, although, due to the presence of the features described above, surface of pores is not smooth. Some cracks, connected to the pores, have been included in the pore vol-

ume by the software. This is observed in Fig. 8, relative to Z2. They affect the larger pore volume intervals.

Fig. 9 illustrates the diagrams of pore-size distribution for the two ZPC samples. The graphs display pores smaller than 300 μm in diameter (order of magnitude 10^4 in number) for sake of clarity. Pores above this size are few (6 pores in Z1 and 33 pores in Z2). The count bars and cumulative curves in Fig. 9 show that pores with diameter <50 μm are more abundant in Z1 sample, while the number of pores with diameter ≥50 μm is higher in Z2 sample, substantially confirming the qualitative observations based on the slices and 3-D renderings (Figs. 5–8). It should be noted that the maximum pore diameter detected is 550 μm and 750 μm for Z1 and Z2 samples, respectively.

Table 4 summarizes the microstructural parameters obtained from SANS and XmCT, together with the results of compressive strength tests. Porosity is given as the percent-
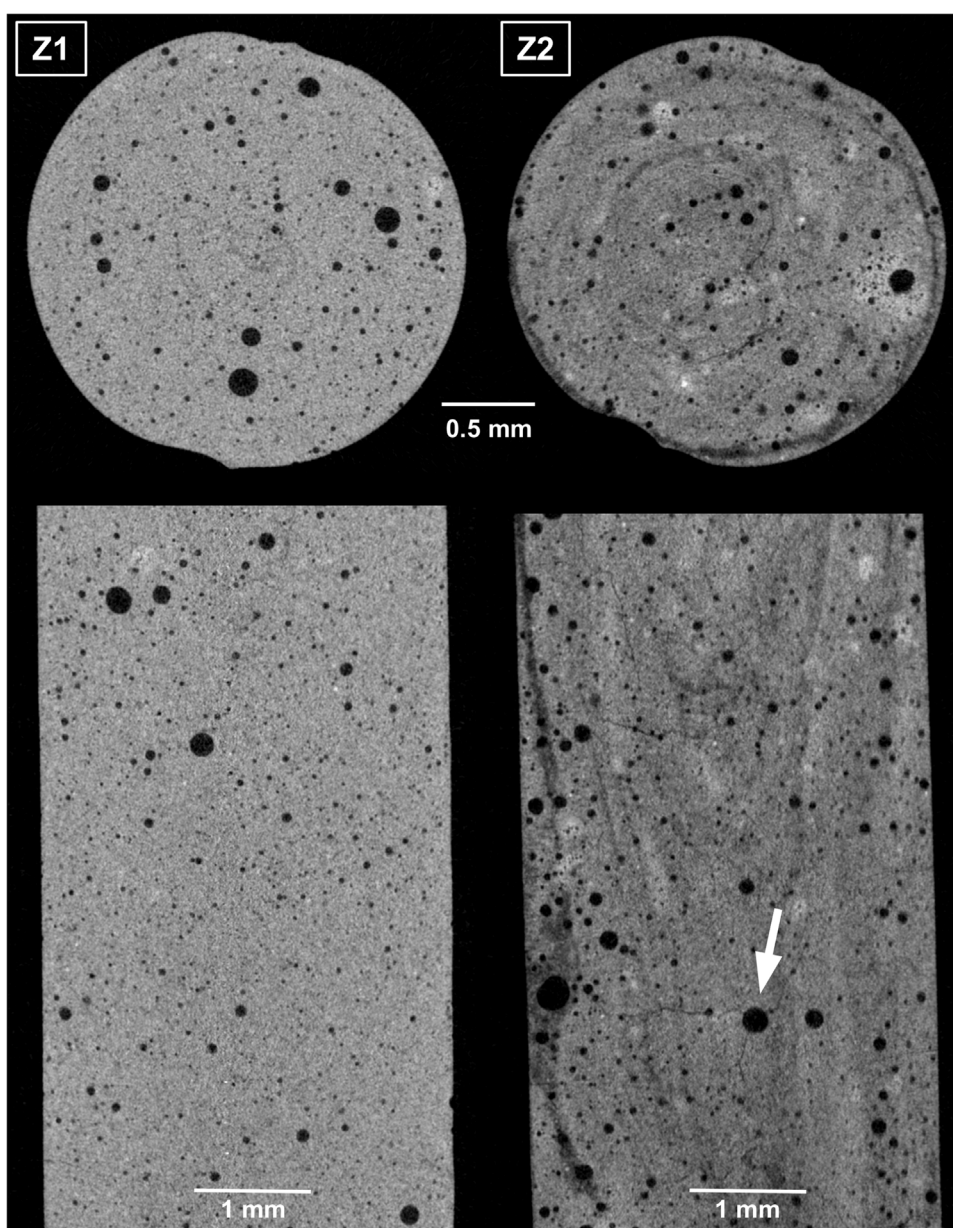

Fig. 5 – Axial (upper part) and coronal (lower part) 2-D XmCT views of ZPC samples. Arrow indicates a large pore with cracks departing from it.

Table 4 – S_V and porosity obtained from SANS and XmCT and compressive strength values.

Sample	SANS		XmCT		Compressive strength (MPa)
	S_V (m^{-1})	Porosity[a] (%)	S_V (m^{-1})	Porosity[a] (%)	
Z1	$11 \times 10^6 \pm 1 \times 10^2$	0.72 ± 0.1	6.7×10^3	3.8	50 ± 3
Z2	$25 \times 10^6 \pm 2 \times 10^2$	1.10 ± 0.1	8.6×10^3	5.2	39 ± 3

[a] Percentage of the volume of pores to the total sample volume.
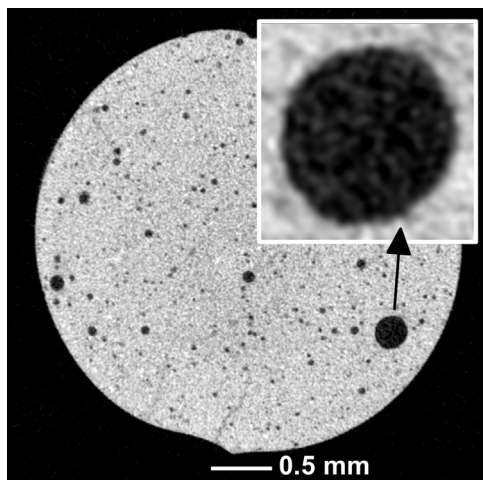
Fig. 6 – Detail from an axial XmCT slice showing a pore containing features (dark gray) with irregular pseudo-dendritic shape in the volume.

age of the volume of pores in the investigated volume (solid plus pores). In case of XmCT, volume of pores was computed as explained in Section 2.2 and no standard deviation on the results is obtained from this procedure. For SANS results, the standard deviations are obtained during the fit of the curves [45], thus, they are inherent to the procedure of calculus and are not related to the average of more sample replicates. On the contrary, for compressive strength, the standard deviation was obtained from the average of 5 sample replicates. The compressive strength results highlight the better performance of formulation Z1 (50 MPa) with respect to Z2 (39 MPa).

4. Discussion

This investigation, intended as a contribution to elucidate a complex matter such as the relationship between microstructure and compressive strength in ZPCs, possesses necessarily several limitations, which include: the study of cement from only one manufacturer; only two l/s values have been tested; influence of different mixing methods was not tested; SANS and XmCT have been conducted on a single sample replicate; voids have been treated as spherical; microstructural characterization was focused on the bulk, neglecting the contribution of surfaces to the cement properties; the choice of compressive strength test in place of, or in addition to, shear or flexural strength tests to evaluate mechanical performance; only 'fresh' specimens have been investigated; effects of exposure to potentially aggressive environments, as the oral environment, have not been tested.

4.1. ZnO powder

The characterization of the powder component of the investigated ZPC indicates that Mg, Al and B have been added to the zinc oxide powder before thermal treatment, because Mg entered the structure of zincite and contributed to the crystallization of kotoite, and Al reacted with ZnO to form the Zn spinel phase (Table 2). A fraction of Mg was hosted in the spinel structure too (Fig. 1b), owing to the complete miscibility between the two end-members in the MgAl$_2$O$_4$–ZnAl$_2$O$_4$ system [53]. The effects of annealing at high temperature are evident in the smooth surface, compactness and coalescence of the ZnO grains, reflecting a high degree of sintering (Fig. 1a) [54]. It has been shown that, at temperatures above 1000 °C, a substantial increase of mean grain size of ZnO, accompanied by a higher degree of crystallinity and increase in density, occurs [54]. In fact, the crystallite size value obtained from the Rietveld refinement of ZnO in the ZPC powder is about six times larger than that of the chemical grade ZnO (Table 3). The small amount of amorphous detected in the ZPC powder agrees with the effect of high temperature annealing on metal oxide powders [55]. The unit-cell parameters of zincite are affected by the incorporation of Mg into the crystal structure. Studies on synthesized Mg$_x$ Zn$_{1-x}$O$_2$ showed that cell parameter **a** increases, while the **c** axis length decreases with increasing Mg content [56,57]. By comparing the refined values (Table 3) with published data [56], it can be argued that the content in Mg of zinc oxide should be comprised between 0.2 and 0.3 mol%. The collected experimental evidences point to annealing temperatures for ZPC powder comprised between 1100 and 1400 °C, but, in consideration of the use of a fluxing agent, more likely towards the lower end of this range. This agrees with previous findings [58]. In fact, crystallization of kotoite should be ascribed to the addition of boron as flux. The amount of this phase corresponds to about 2.38 wt% of B$_2$O$_3$. Being easily synthesized from B$_2$O$_3$ at temperatures as low as 800 °C [59], it is not indicative of the annealing temperature attained. It is clear that the phase composition of the powder and the microstructure of ZnO particles after thermal treatment have been designed to improve the characteristics of workability and performance of the cement. Therefore, they impacted directly on the setting reaction and the cement microstructure, as discussed in the next section.

4.2. ZPC composition

The QPA carried out on the ZPC samples confirms that in Al modified systems the product of reaction is completely amorphous and crystallization is effectively inhibited [10,11]. Diffraction peaks of hopeite or other crystalline zinc phosphates were not detected in our case. Considering that QPA
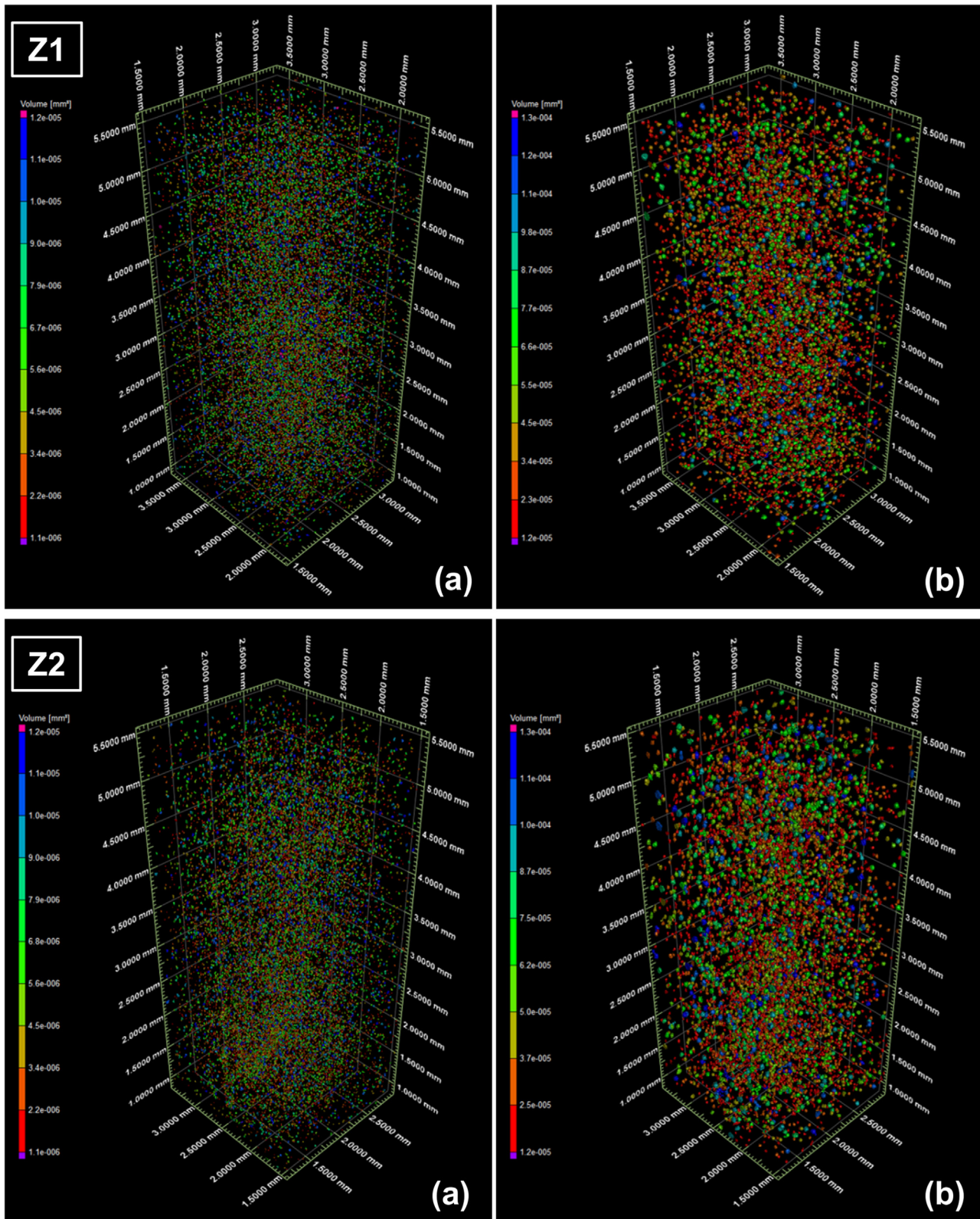
Fig. 7 – 3-D visualisation of porosity distribution in ZPC samples for the volume intervals 1.1×10^{-6}–1.2×10^{-5} mm^3 (a) and 1.2×10^{-5}–1.3×10^{-4} mm^3 (b), corresponding to diameter intervals 0.01–0.02 mm and 0.02–0.05 mm, respectively. The pores are described as objects of different color, according to their volume size.
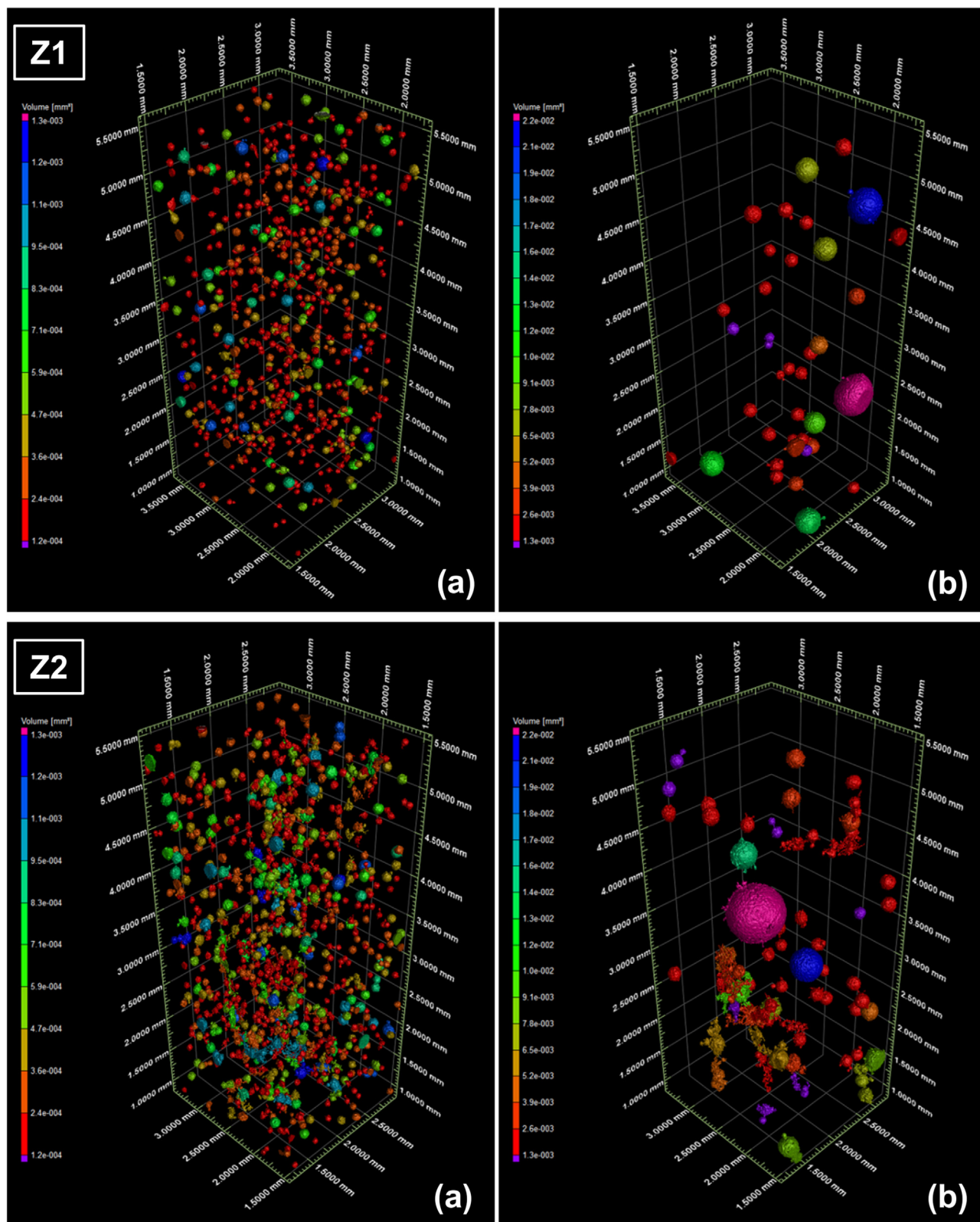
Fig. 8 – 3-D visualization of porosity distribution in ZPC samples for the volume intervals 1.2×10^{-4}–1.3×10^{-3} mm^3 (a) and 1.3×10^{-3}–2.2×10^{-2} mm^3 (b), corresponding to diameter intervals 0.05–0.11 mm and 0.11–0.28 mm, respectively. The pores are described as objects of different color, according to their volume size.
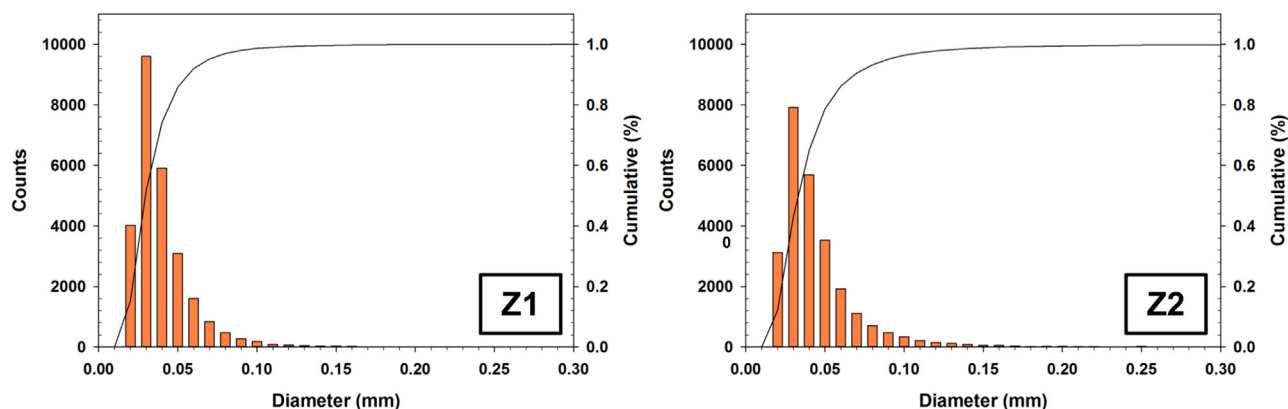
Fig. 9 – Pore-size distribution in samples Z1 (a) and Z2 (b) illustrated as counts bars and cumulative curve.

and SEM observations were conducted after the other tests, significant effects due to hopeite crystallization on sample microstructure, can be reasonably excluded. The increase of about 10.6 wt% of liquid in the mix for sample Z2, resulted in almost the same increase in the weight fraction of the amorphous product. MgO in the powder is expected to be involved in the reaction with the acid phosphate solution in a similar way as during formation of Mg phosphate cements, yielding an amorphous product [6]. This explains why, having considered the dilution due to the addition of the liquid component, its content is lower than expected (0.9 and 0.8 wt% in Z1 and Z2, respectively). The same does not happen for gahnite, whose expected content (2.0 and 1.8 wt% in Z1 and Z2, respectively) is similar to the detected one. Therefore, the fractions of Al and Zn hosted in the spinel phase are effectively subtracted to the main setting reaction. The fraction of kotoite is sensibly lower than expected (4.5 and 3.9 wt% in Z1 and Z2, respectively). This is explained by its partial dissolution in the acidic environment [60]. It follows that, since boron available in solution is known to act as retardant in the reaction of acid–base cements [61,62], it likely played the double role of flux (during powder annealing) and retardant (during setting). The microstructural features accessible by SEM confirm previous results about the shape of pores obtained with optical methods [25,27], but the indication of higher porosity in the sample with higher l/s, seems at variance with previous findings [16] and will be discussed further in the light of the SANS and XmCT results. The observed good contact of the matrix with the ZnO grains, and the corrosion features at the grain surfaces, agrees with previous SEM observations [63] and testify the effect of dissolution process triggered by the contact with the acid phosphate solution.

4.3. SANS interpretation

SANS curves of both ZPC samples show three regions in accordance with reports on materials showing hierarchical levels of scattering objects [64]. As indicated in Fig. 3, at low Q the scattering follows a Guinier regime [41] that is only partially resolved because of the experimental Q range accessed. At intermediate Q ($\sim$0.2 nm^{-1}) a second Guinier regime can be recognized. This is followed by a region at high Q showing a

power law regime. Between the two Guinier regimes no intermediate power law regime can be resolved; here, the slope of the SANS curve gives exponent everywhere higher than 4. Such behavior can be ascribed to the overlapping of the two Guinier regimes, in consequence of the size distribution of scattering objects.

When the different contributions to the scattered intensity are considered, it must be noted that, according to the description of powder systems [65], the contribution to the scattering of the form factor of grains, providing information on the shape and size of objects, when grains have micrometric size, is experimentally accessible only at very low values of Q. For the ZnO grains, this region is outside the experimental Q range. Therefore, it can be argued that the experimental curves are describing the contribution of the surface of pores in the matrix and within the grains [65]. Since there is no evidence of porosity in the ZnO grains (as a consequence of powder processing), this component can be neglected. The same applies to the other powder fractions, accounting for less than 6 wt% (Table 2). It follows that the interface giving rise to the measured scattered intensity can be assumed to be that of the pores in the amorphous matrix.

4.4. SANS analysis

The application of the mathematical models to retrieve quantitative information on the system relies on the choice of the shape of scattering objects and value of scattering contrast. For the latter, this means to know the composition and density of the solid matrix and fluid in pores. On the basis of previous experimental evidences, the composition of the amorphous matrix was assumed $Zn_2P_4O_{12}\cdot 8H_2O$ [11] and its density that of the crystalline counterpart (2.44 g/cm^3), with which the compound shares the same structural units [66]. Being boron a neutron absorber, its content was also considered in the calculation.

As far as the composition of the fluid in pores is concerned, the reports on porosity in water-based dental cements points to water-filled nano-pores [16,27], since water is in excess in the solution. This view agrees with the detected water loss

in ZPCs [67]. The fit of the power law regime in the Q range 0.025–3 nm^{-1} with the expression:

$$I(Q) = B\left(\frac{1}{Q}\right)^n + C \qquad (4)$$

gave exponent 4.15 and 3.98 for Z1 and Z2, respectively. This allowed us to apply Eq. (3) (Porod regime) to derive S_V of the population of the smallest pores. The obtained values are reported in Table 4. They are comparable to those measured in sintered ceramic materials [34] and Mg phosphate cements [31,35], with sample Z2 showing higher S_V with respect to Z1.

The SANS data have been fitted with the Monte Carlo method using the sphere model for the shape of pores and the scattering contrast calculated as described above. According to the indications from XmCT on the larger porosity, and as common practice in the analysis of the microstructure of ceramics [34], a spherical shape of micro-pores was assumed. From the results of fit (Fig. 3) the volume-weighted size distributions of pores have been derived (Fig. 4). Both samples show similar bimodal distributions with two populations of pores with radius centered at around 20 nm and 200 nm. The values are higher for sample Z2, with a bigger difference for the smallest pores.

4.5. ZPC microstructure

The microstructural differences between the two ZPC samples can be interpreted in the light of their different l/s ratio. The fine porosity in ZPCs, due to pores of about 5 μm in diameter, has been reported to develop from the entrapment of excess water [28]. This trend seems to be confirmed for the ultrafine porosity accessible with SANS ($D < 200$ nm). Results indicate that it is more developed in the sample Z2, prepared with higher l/s. The first maximum in the SANS pore-size distribution at 20 nm is in line with previous MIP results [28], obtained on ZPC with l/s = 0.56, a value similar to that of Z2. In that work, the sample also showed a bimodal distribution with a second maximum at $200 < D < 500$ nm. It is worth noting that, for the two compositions investigated, the position of the maxima of the bimodal distribution seems not to be affected by l/s. This means that the viscosity of the paste is playing a minor role in influencing the size of pores with $D < 200$ nm. Conversely, the increase in the amount of liquid brought about an increase in the number of mesopores ($2 < D < 50$ nm). Therefore, segregation of liquid seems to be a mechanism behind the development of micro-porosity in ZPC. It should be noted that previous investigations adopting optical methods, could not access the porosity below 1 μm [16,25,27].

Experiments conducted at different mixing ratios, have shown that the number of pores above 6 μm increased increasing the powder fraction [16]. This was explained with the formation of agglomerates of zinc oxide particles containing voids during mixing, or air-entrapment when filling the mold. Furthermore, water, although recognized to be present in the cement, was not considered to play a role in pore formation. Therefore, higher liquid content was expected to provide a more homogeneously hardened material. This range in pore size is covered, in a fully non-invasive fashion, by XmCT; in fact, the images reported in Fig. 5, and the corre-

sponding 3-D renderings (Figs. 7 and 8) seem to contradict this assumption. In addition, the results show that 50 μm is a niche pore-size value, which allows to distinguish the two ZPC samples in terms of porous structure. The increase in l/s ratio resulted in a larger fraction of pores with $D \gtrsim 50$ μm (21.3% in Z2, against 14.1% in Z1) and, more in general, in the formation of larger pores, as described in Section 3 and graphically depicted in Fig. 9. Consequently, the total porosity and the XmCT derived S_V increased, increasing the amount of liquid (Table 4). Together with the inferior mechanical performance, this is consistent with findings suggesting that large pores more readily occur in lower viscosity materials, reducing the strength [24]. Such pores were, however, considered air inclusions, formed during the preparation of the cement, thus, more affected by mixing method and/or operator-dependent.

XmCT may help to shed new light on this point. The distinctive features observed inside the pores of both samples and on their surface (Fig. 6), point to the precipitation/crystallization of material with density on average lower than the matrix. This must have occurred when pores were already formed and, necessarily, in presence of a liquid phase. It must be pointed out that the experimental conditions of this XmCT investigation prevented from the direct detection of liquid water inside the pores. Lower X-ray energy and the use of synchrotron light, capable of exploiting higher phase contrast, should be employed at the scope, and will be considered for future investigations. This would also allow to quantitatively analyze pores with sizes in the range from 1 to 10 microns. It follows, that we cannot prove the presence of water in the pores in the present case, but we can reasonably infer that the liquid was filling the pores when they formed, allowing for the precipitation of a reaction product.

The proposed mechanism is that, at the beginning, the reaction is driven by the dissolution of ZnO grains making available the metal ions for the formation of the amorphous product [6,11]. A large volume of cement is formed quickly, consuming phosphate ions and a large fraction of water. This process hinders further contact of ZnO grains with the liquid, which, at the same time, becomes progressively depleted in phosphate, thus, less reactive. In Al-modified ZPCs, this hindering effect is enhanced by the condensation of the aluminophosphate hydrogel coating the ZnO particles [11]. The remaining fraction of unreacted liquid is segregated into pores and their number and size should depend, amongst other aspects (e.g. mixing conditions) from the viscosity of the paste and l/s (which are interdependent parameters). The pore solution still preserves a residual reactivity, and it can be argued that a small amount of reaction product precipitates at the matrix/pore interface (i.e. at the surface of pores) and in the pore volume, as indicated by XmCT. During this late stage the rest of phosphorous can be consumed in a sluggish process, as the NMR signal of unreacted phosphoric acid was still detected after 2 days [13]. Unlike older samples, in these cements aged 48 h, ^{31}P NMR showed more than one resonance, suggesting that phosphorous was present in more than one hydrated environment. Other authors have come to the same conclusion from the results of dissolution tests [68]. It is thus conjectured that the material precipitating in pores is an intermediate, highly hydrated (probably gel-like) precursor of the

main ZPC reaction product, a view compatible with the mechanism proposed for the chemical evolution of ZPCs [11]. Such highly hydrated, less compact product, which, depending on the chemical-physical environment, may later convert into the main ZPC reaction product, can explain the features observed with XmCT.

The presence of this material in pores of all sizes lead us to reconsider the theories invoking air-entrapment as main cause of development of large porosity in ZPCs [16,27]. A high liquid content seems to have also favoured inhomogeneities in the matrix, as observed in the sections reported in Fig. 5. They reflect changes in density whose nature seems directly related to the irregular distribution of the liquid and solid fractions. In Z2, the volumes of sample showing lower contrast (low Iso values) are interested by a higher concentration of pores, as depicted in the lower left part of the longitudinal section and in the external ring of the transverse section in Fig. 5. This could be the result of a local increase in the liquid fraction. At the same time, volumes with higher contrast (Iso values similar to the matrix in Z1), can be also recognized. They identify a higher concentration of ZnO grains. It can be concluded that the higher amount of liquid favoured the development of microstructural and compositional inhomogeneities during mixing. They were preserved during casting, appearing in shape of flow marks, indicating the direction of material flow.

4.6. ZPC performance

The compressive strength values obtained in the present work are below (Z2) or at (Z1) the minimum limit recommended in EN ISO 9917-1:2007 [39]. This does not mean that the samples are not representative of the restorative materials used in clinical practice. The compressive strength values of ZPCs produced by 40 different operators showed significant dispersion, with a considerable fraction of samples falling below 50 MPa [15]. The values of samples Z1 and Z2 are in accordance with those reported in this study for similar l/s ratios. In general, a direct comparison between different studies is hampered by the lack of uniformity in testing methods and by the intra-operator variability observed between laboratories adopting the ISO standard [69]. According to the findings of Fleming et al. [16], the mixing ratio of sample Z1 should be in excess of powder component, favoring the development of agglomerates and large pores (>40 μm), resulting in a poorly performant cement. However, this sample is more performant than Z2. It should be observed that the experimental evidences about the relationship between mechanical properties and l/s are sometimes conflicting. The reason is that the correlation between mixing ratio and performance is mediated by the behavior of the cement components during the setting reaction. Different cements with same mixing ratio can display different properties, an aspect to be considered when comparing different commercial products. Our characterization of the powder component showed that several variables (annealing time and temperature, introduction of Mg, Al, B) can be used by the producers to influence cement behavior during the setting reaction. For example, acting on the reaction kinetics, more liquid could be made available and for more time. This can be done by modifying the specific reactivity of the powders or its grain-size distribution (e.g. longer dwell

time, annealing at higher temperature, adding flux to increase sintering), synthesizing an inert phase not involved in the reaction (e.g. spinel in the studied system), include a retarder (e.g. boron compounds). The rheology of the cement pastes will be strongly affected and, consequently, also the number and size distribution of water-filled pores or grain aggregates during mixing. In the investigated ZPCs, performance seems to be directly related to the porosity, and, as the porosity seems to develop predominantly through segregation of liquid rather than by air-entrapment during mixing, the increase in l/s should be considered the main parameter affecting the measured compressive strength. We are conscious that the relationship between porosity and strength should take into consideration the pore/size distribution rather than the total vol.% of pores. In fact, in the studied samples the increase of l/s results in a general increase in porosity but also in the relative fraction of the largest pores (with $D \geq 50\,\mu m$), and large pores are expected to impact more on the resulting strength of the ceramic, as being theoretically the most detrimental. The cracks detected in the matrix of sample Z2 might have further contributed in decreasing its compressive strength. Their nature is not clear, it could be related to tensile stress concentration around the pores [21–23,70], as the example highlighted in Fig. 5 might indicate, or to residual stress due to contraction [71,72]. According to literature [72], in the latter case, they might have been much less developed in the samples employed for compressive strength tests, because aged in water. The fact that cracks are more evident in the sample with higher l/s agrees with the intervention of shrinkage, since it was observed to be more pronounced at higher liquid content.

Porosity and S_V play a role when the resistance to erosion (chemical attack), staining potential or fluoride release/uptake of the cement are considered [27,68,73–75]. The latter has been recognized to be more surface than bulk-dependent. For this reason S_V is a useful diagnostic parameter. As evidenced in Table 4, S_V is largely contributed by the finest porosity, but of more relevance is that the difference between the two samples is much larger in the range of porosity covered by SANS than in that covered by XmCT. This highlights the importance of SANS derived S_V for understanding the properties of the cement. The formulation recommended as filling material (Z1) is potentially less active with respect to fluoride release/uptake, and less resistant to dissolution, a process recognised to be more effective on the unreacted powder component (filler) rather than on the matrix [68]. It is evident from the above discussion that the combined use of SANS and XmCT conveyed new information on the sample microstructure, with implications for the properties of this class of dental materials. Both methods complement each other not only because of the wide range in pore size covered, part of which is hardly accessible with other techniques, but also owing to the different level of the retrieved information. The pores with $0.2 < D < 10\,\mu m$, which could not be detected in the experimental conditions employed in the present investigation, can be accessed either by working with different SANS instruments or with high resolution synchrotron XmCT measurements. Further investigations to confirm and complement the results obtained in this work may include:

- The investigation of a larger number of cements including more manufacturers and mixing ratios.
- The microstructural characterization of samples prepared with different mixing methods.
- The study of samples exposed to potentially aggressive environments.
- The investigation of the release-uptake properties in function of S_V and l/s.
- The investigation of the state of water (free or liquid, and bound) in the cement using neutron quasi elastic scattering.

The latter study is in progress, and is also aimed at confirming the nature of porosity and quantify the amount of water in pores.

5.   Conclusions

The investigation of the powder component of the ZPCs showed that reactivity was modulated by annealing and introducing Mg, Al and B. The beneficial effects obtained by the addition of Al and Mg to improve sintering were mitigated by the crystallization of a Zn aluminate phase not involved in the setting reaction.

Both cements showed sub-spherical pores attributed to liquid segregation. Increasing the liquid fraction increases total porosity and the relative fraction of largest pores, with detriment for the mechanical properties.

The specific surface area is lower for the formulation recommended as filling material (lower liquid content). Therefore, this formulation should be less active with respect to fluoride release/uptake (surface dependent), and it should show a higher dissolution rate, because of the higher fraction of unreacted ZnO powder.

Acknowledgments

Appendix A. Supplementary data

Supplementary data associated with this article can be found, in the online version, at http://dx.doi.org/10.1016/j.dental.2017.01.008.

REFERENCES

[1] Gerlach A, Vincent B, Lissac M, Esnouf X, Thollet G. Distribution of zinc ions from orthophosphate cements at the cement-tooth interface in fixed dental prosthesis. Biomaterials 1993;14:770–4, http://dx.doi.org/10.1016/0142-9612(93)90042-Z.

[2] Pameijer CH. A review of luting agents. Int J Dent 2012;2012:752861, http://dx.doi.org/10.1155/2012/752861.

[3] Jefferies SR. Bioactive and biomimetic restorative materials: a comprehensive review. Part II. J Esthet Restor Dent 2014;26:14–26, http://dx.doi.org/10.1111/jerd.12066.

[4] Jokstad A. A split-mouth randomized clinical trial of single crowns retained with resin-modified glass-Ionomer and zinc phosphate luting cements. Int J Prosthodont 2004;17:411–6.

[5] Wacker DR, Tjan AHL. Effect of variation in powder-to-liquid ratio of zinc phosphate cement on the retention of posts. J Prosthet Dent 1988;60:49–52, http://dx.doi.org/10.1016/0022-3913(88)90349-6.

[6] Wilson A, Nicholson JW. Acid-base cements. Cambridge University Press; 1993.

[7] Viani A, Peréz-Estébanez M, Pollastri S, Gualtieri AF. In situ synchrotron powder diffraction study of the setting reaction kinetics of magnesium-potassium phosphate cements. Cem Concr Res 2016;79:344–52, http://dx.doi.org/10.1016/j.cemconres.2015.10.007.

[8] Louer D, Vargas R, Auffredic J-P. Morphological analysis and growth of crystallites during annealing of ZnO. J Am Ceram Soc 1984;67:136–41, http://dx.doi.org/10.1111/j.1151-2916.1984.tb09631.x.

[9] Li D, Haneda H. Morphologies of zinc oxide particles and their effects on photocatalysis. Chemosphere 2003;51:129–37, http://dx.doi.org/10.1016/S0045-6535(02)00787-7.

[10] Park C-K, Silsbee M, Roy D. Setting reaction and resultant structure of zinc phosphate cement in various orthophosphoric acid cement-forming liquids. Cem Concr Res 1998;28:141–50, http://dx.doi.org/10.1016/S0008-8846(97)00223-8.

[11] Pawlig O, Trettin R. In-situ DRIFT spectroscopic investigation on the chemical evolution of zinc phosphate acid-base cement. Chem Mater 2000;12:1279–87.

[12] O'Neill IK, Prosser HJ, Richards CP, Wilson AD. NMR spectroscopy of dental materials. I.31P studies on phosphate-bonded cement liquids. J Biomed Mater Res 1982;16:39–49, http://dx.doi.org/10.1002/jbm.820160107.

[13] Margerit J, Cluzel B, Leloup JM, Nurit J, Pauvert B, Terol A. Chemical characterization of in vivo aged zinc phosphate dental cements. J Mater Sci Mater Med 1996;7:623–8, http://dx.doi.org/10.1007/BF00058202.

[14] Marshall GW, Marshall SJ, Bayne SC. Restorative dental materials: scanning electron microscopy and x-ray microanalysis. Scanning Microsc 1988;2:2007–28.

[15] Fleming GJ, Marquis P, Shortall AC. The influence of clinically induced variability on the distribution of compressive fracture strengths of a hand-mixed zinc phosphate dental cement. Dent Mater 1999;15:87–97, http://dx.doi.org/10.1016/S0109-5641(99)00018-4.

[16] Fleming GJ, Shelton R, Landini G, Marquis P. The influence of mixing ratio on the toughening mechanisms of a hand-mixed zinc phosphate dental cement. Dent Mater 2001;17:14–20, http://dx.doi.org/10.1016/S0109-5641(00)00044-0.

[17] Walton TR. The flow properties of zinc phosphate cement: an argument for changing the standard. Aust Dent J 1980;25:215–8, http://dx.doi.org/10.1111/j.1834-7819.1980.tb03868.x.

[18] Wilder AD, Boghosian AA, Bayne SC, Heymann HO, Sturdevant JR, Roberson TM. Effect of powder/liquid ratio on the clinical and laboratory performance of resin-modified glass-ionomers. J Dent 1998;26:369–77, http://dx.doi.org/10.1016/S0300-5712(97)00018-3.

[19] Gonzaga CC, Cesar PF, Miranda WG, Yoshimura HN. Slow crack growth and reliability of dental ceramics. Dent Mater 2011;27:394–406, http://dx.doi.org/10.1016/j.dental.2010.10.025.

[20] Swain MV. Toughening mechanisms for ceramics. Mater Forum 1989;13:237–53, http://dx.doi.org/10.1016/B978-1-4832-8382-1.50173-7.

[21] Rice RW. Pores as fracture origins in ceramics. J Mater Sci 1984;19:895–914, http://dx.doi.org/10.1007/BF00540460.

[22] Kelly JR, Campbell SD, Bowen HK. Fracture-surface analysis of dental ceramics. J Prosthet Dent 1989;62:536–41, http://dx.doi.org/10.1016/0022-3913(89)90075-9.

[23] Danzer R, Lube T, Supancic P, Damani R. Fracture of ceramics. Adv Eng Mater 2008;10:275–98, http://dx.doi.org/10.1002/adem.200700347.

[24] Nomoto R, Komoriyama M, McCabe JF, Hirano S. Effect of mixing method on the porosity of encapsulated glass ionomer cement. Dent Mater 2004;20:972–8, http://dx.doi.org/10.1016/j.dental.2004.03.001.

[25] Mitchell CA, Douglas WH. Comparison of the porosity of hand-mixed and capsulated glass-ionomer luting cements. Biomaterials 1997;18:1127–31, http://dx.doi.org/10.1016/S0142-9612(97)00038-0.

[26] Rouquerol J, Avnir D, Fairbridge CW, Everett DH, Haynes JM, Pernicone N, et al. Recommendations for the characterization of porous solids (technical report). Pure Appl Chem 1994;66, http://dx.doi.org/10.1351/pac199466081739.

[27] Bertenshaw BW, Piddock V. Porosity in water-based dental luting cements. J Mater Sci Mater Med 1993;4:415–7, http://dx.doi.org/10.1007/BF00122201.

[28] Milutinović-Nikolić AD, Medić VB, Vuković ZM. Porosity of different dental luting cements. Dent Mater 2007;23:674–8, http://dx.doi.org/10.1016/j.dental.2006.06.006.

[29] Diamond S. Mercury porosimetry. An inappropriate method for the measurement of pore size distributions in cement-based materials. Cem Concr Res 2000;30:1517–25, http://dx.doi.org/10.1016/S0008-8846(00)00370-7.

[30] de With G, Glass HJ. Reliability and reproducibility of mercury intrusion porosimetry. J Eur Ceram Soc 1997;17:753–7, http://dx.doi.org/10.1016/S0955-2219(96)00181-1.

[31] Viani A, Sotiriadis K, Šašek P, Appavou M-S. Evolution of microstructure and performance in magnesium potassium phosphate ceramics: role of sintering temperature of MgO powder. Ceram Int 2016;42:16310–6, http://dx.doi.org/10.1016/j.ceramint.2016.07.182.

[32] United Nations Environment Programme. Text of the Minamata Convention on Mercury for adoption by the Conference of Plenipotentiaries. The Conference of Plenipotentiaries on the "Minamata Convention on Mercury" 2013:1–31. http://www.unep.org/hazardoussubstances/Portals/9/Mercury/Documents/dipcon/CONF… [Accessed 10 March 2016].

[33] Williams JA, Billington RW, Pearson GJ. The influence of sample dimensions on fluoride ion release from a glass ionomer restorative cement. Biomaterials 1999;20:1327–37.

[34] Allen AJ, Krueger S, Long GG, Kerch HM, Hahn H, Skandan G. Small-angle neutron scattering studies of ceramic nanophase materials. Nanostruct Mater 1996;7:113–26, http://dx.doi.org/10.1016/0965-9773(95)00314-2.

[35] Viani A, Radulescu A, Peréz-Estébanez M. Characterisation and development of fine porosity in magnesium potassium

phosphate ceramics. Mater Lett 2015;161:628–30, http://dx.doi.org/10.1016/j.matlet.2015.09.056.

[36] Swain MV, Xue J. State of the art of Micro-CT applications in dental research. Int J Oral Sci 2009;1:177–88, http://dx.doi.org/10.4248/IJOS09031.

[37] Benetti AR, Jacobsen J, Lehnhoff B, Momsen NCR, Okhrimenko DV, Telling MTF, et al. How mobile are protons in the structure of dental glass ionomer cements? Sci Rep 2015;5:8972, http://dx.doi.org/10.1038/srep08972.

[38] De Santis R, Mollica F, Prisco D, Rengo S, Ambrosio L, Nicolais L. A 3D analysis of mechanically stressed dentin-adhesive-composite interfaces using X-ray micro-CT. Biomaterials 2005;26:257–70, http://dx.doi.org/10.1016/j.biomaterials.2004.02.024.

[39] European Committee for Standardization. Dentistry — water-based cements — part 1: powder/liquid acid-base cements. EN ISO 9917-1:2007. CEN/TC 55 — dentistry, 2007.

[40] Radulescu A, Szekely N, Appavou M-S. KWS-2: small angle scattering diffractometer. J Large-Scale Res Facil JLSRF 2015;1:29, http://dx.doi.org/10.17815/jlsrf-1-27.

[41] Glatter O, May R. Small-angle techniques. In: International Tables for Crystallography. Dordrecht: Kluwer Academic Publishers; 1999.

[42] Hardman-Rhyne K, Berk NF, Fuller ER. Microstructural characterization of ceramic materials by small angle neutron scattering techniques. J Res Natl Bur Stand (1934) 1984;89:17, http://dx.doi.org/10.6028/jres.089.003.

[43] Allen AJ. Characterization of ceramics by X-ray and neutron small-angle scattering. J Am Ceram Soc 2005;88:1367–81, http://dx.doi.org/10.1111/j.1551-2916.2005.00463.x.

[44] Porod G. General theory. In: Glatter O, Kratky O, editors. Small-angle X-ray scattering. London: Academic Press; 1982. p. 17–51.

[45] Bressler I, Pauw BR, Thünemann AF. McSAS: software for the retrieval of model parameter distributions from scattering patterns. J Appl Crystallogr 2015;48:962–9, http://dx.doi.org/10.1107/S1600576715007347.

[46] Zandomeneghi D, Voltolini M, Mancini L, Brun F, Dreossi D, Polacci M. Quantitative analysis of X-ray microtomography images of geomaterials: application to volcanic rocks. Geosphere 2010;6:793–804, http://dx.doi.org/10.1130/GES00561.1.

[47] Elettra — Sincrotrone Trieste S.C.p.A. TomoLab n.d. http://www.elettra.trieste.it/lightsources/labs-and-services/tomolab/tomolab.html. [Accessed 26 July 2016].

[48] Wilkins SW, Gureyev TE, Gao D, Pogany A, Stevenson AW. Phase-contrast imaging using polychromatic hard X-rays. Nature 1996;384:335–8, http://dx.doi.org/10.1038/384335a0.

[49] Cloetens P, Barrett R, Baruchel J, Guigay J-P, Schlenker M. Phase objects in synchrotron radiation hard x-ray imaging. J Phys D Appl Phys 1999;29:133–46, http://dx.doi.org/10.1088/0022-3727/29/1/023.

[50] Brun F, Mancini L, Kasae P, Favretto S, Dreossi D, Tromba G. Pore3D: a software library for quantitative analysis of porous media. Nucl Instruments Methods Phys Res. Sect A Accel Spectrometers, Detect Assoc Equip 2010;615:326–32, http://dx.doi.org/10.1016/j.nima.2010.02.063.

[51] Brun F, Kourousias G, Dreossi D, Mancini L. An improved method for ring artifacts removing in reconstructed tomographic images. In: Dössel O, Schlegel WC, editors. IFMBE Proceedings. Berlin: Springer Berlin Heidelberg; 2009. p. 926–9, http://dx.doi.org/10.1007/978-3-642-03882-2_247.

[52] Verein deutscher Gießereifachleut. Volumendefizite von Gußstücken aus Nichteisenmetallen, VDG P201. Verein deutscher Gießereifachleut; 2002. Düsseldorf, P201.

[53] Petrova MA, Mikirticheva GA, Novikova AS, Popova VF. Spinel solid solutions in the systems $MgAl_2O_4$–$ZnAl_2O_4$ and

MgAl$_2$O$_4$–Mg$_2$TiO$_4$. J Mater Res 1997;12:2584–8, http://dx.doi.org/10.1557/JMR.1997.0343.

[54] Ishii T. Surface reactivity of oxide powders in the solid-solid reaction systems bearing zinc oxide by emanation thermal analysis. React Solids 1988;6:1–10, http://dx.doi.org/10.1016/0168-7336(88)80041-X.

[55] Eubank WR. Calcination studies of magnesium oxides. J Am Ceram Soc 1951;34:225–9, http://dx.doi.org/10.1111/j.1151-2916.1951.tb11644.x.

[56] Kim Y-I, Page K, Seshadri R. Synchrotron x-ray study of polycrystalline wurtzite Zn[sub 1-x]Mg[sub x]O (0 ≤ x ≤ 0.15): evolution of crystal structure and polarization. Appl Phys Lett 2007;90:101904, http://dx.doi.org/10.1063/1.2711289.

[57] Ohtomo A, Kawasaki M, Koida T, Masubuchi K, Koinuma H, Sakurai Y, et al. Mg[sub x]Zn[sub 1-x]O as a II-VI widegap semiconductor alloy. Appl Phys Lett 1998;72:2466, http://dx.doi.org/10.1063/1.121384.

[58] Pawlig O, Trettin R. Applications of conduction calorimetry to the setting reaction of zinc phosphate dental cement. Thermochim Acta 1999;329:7–15, http://dx.doi.org/10.1016/S0040-6031(99)00008-8.

[59] Effenberger H, Pertlik F. Verfeinerung der Kristallstrukturen der isotypen Verbindungen M3(BO3)2 mit M=Mg, Co und Ni (Strukturtyp: Kotoit). Zeitschrift Für Krist: Cryst Mater 1984;16:6, http://dx.doi.org/10.1524/zkri.1984.166.14.129.

[60] Kotoit Watanabe T. ein neues gesteinsbildendes Magnesiumborat. Zeitschrift Für Krist Mineral Und Petrogr 1938;50:441–63.

[61] Wagh AS, Jeong SY. Chemically bonded phosphate ceramics: I, A dissolution model of formation. J Am Ceram Soc 2003;86:1838–44, http://dx.doi.org/10.1111/j.1151-2916.2003.tb03569.x.

[62] Sugama T, Kukacka LE. Characteristics of magnesium polyphosphate cements derived from ammonium polyphosphate solutions. Cem Concr Res 1983;13:499–506, http://dx.doi.org/10.1016/0008-8846(83)90008-X.

[63] Grant AA, Greener EH, Meshii M. High resolution microscopy of dental cements. Aust Dent J 1968;13:295–301, http://dx.doi.org/10.1111/j.1834-7819.1968.tb03823.x.

[64] Beaucage G, Kammler HK, Pratsinis SE. Particle size distributions from small-angle scattering using global scattering functions. J Appl Crystallogr 2004;37:523–35, http://dx.doi.org/10.1107/S0021889804008969.

[65] Spalla O, Lyonnard S, Testard F. Analysis of the small-angle intensity scattered by a porous and granular medium. J Appl Crystallogr 2003;36:338–47, http://dx.doi.org/10.1107/S0021889803002279.

[66] Averbuch-Pouchot MT. Crystal structure of zinc-tetrametaphosphate octahydrate: Zn$_2$P$_4$O$_{12}$ 8H$_2$O. Zeitschrift Für Anorg Und Allg Chemie 1983;503:231–7, http://dx.doi.org/10.1002/zaac.19835030825.

[67] Nicholson JW, Czarnecka B. The kinetics of water loss from zinc phosphate and zinc polycarboxylate dental cements. J Mater Sci Mater Med 2008;19:1719–22, http://dx.doi.org/10.1007/s10856-007-3269-1.

[68] Czarnecka B, Limanowska-Shaw H, Nicholson JW. Ion-release, dissolution and buffering by zinc phosphate dental cements. J Mater Sci Mater Med 2003;14:601–4, http://dx.doi.org/10.1023/A:1024018923186.

[69] Fleming GJP, Dowling AH, Addison O. The crushing truth about glass ionomer restoratives: exposing the standard of the standard. J Dent 2012;40:181–8, http://dx.doi.org/10.1016/j.jdent.2011.12.004.

[70] Denry I. How and when does fabrication damage adversely affect the clinical performance of ceramic restorations? Dent Mater 2013;29:85–96, http://dx.doi.org/10.1016/j.dental.2012.07.001.

[71] Osman SA, McCabe JF, Walls AW. Polymerisation shrinkage of luting agents for crown and bridge cementation. Eur J Prosthodont Restor Dent 2008;16:39–44.

[72] Øilo G. Linear dimensional change during setting of a zinc phosphate cement. J Oral Rehabil 1975;2:179–85, http://dx.doi.org/10.1111/j.1365-2842.1975.tb01529.x.

[73] Dupuis V, Laviole O, Potin-Gautier M, Castetbon A, Moya F. Solubility and disintegration of zinc phosphate cement. Biomaterials 1992;13:467–70, http://dx.doi.org/10.1016/0142-9612(92)90168-N.

[74] Nomoto R, McCabe J. A simple acid erosion test for dental water-based cements. Dent Mater 2001;17:53–9, http://dx.doi.org/10.1016/S0109-5641(00)00058-0.

[75] Pawluk K, Booth SE, Coleman NJ, Nicholson JW. The interaction of zinc oxide-based dental cements with aqueous solutions of potassium fluoride. J Mater Sci Mater Med 2008;19:3035–9, http://dx.doi.org/10.1007/s10856-008-3443-0.